Electrochimica Acta 320 (2019) 134546

Contents lists available at ScienceDirect

Electrochimica Acta

journal homepage: www.elsevier.com/locate/electacta

Anodic reactions occurring on simulated spent nuclear fuel (SIMFUEL) in hydrogen peroxide solutions containing bicarbonate/carbonate – The effect of fission products

Ziyan Zhu [a], Linda Wu [a], James J. Noël [a, b, *], David W. Shoesmith [a, b]

[a] Department of Chemistry, The University of Western Ontario, London, Ontario, Canada, N6A 5B7
[b] Surface Science Western, The University of Western Ontario, London, Ontario, Canada, N6C 0J3

ARTICLE INFO

Article history:
Received 4 March 2019
Received in revised form
6 July 2019
Accepted 14 July 2019
Available online 15 July 2019

Keywords:
Spent nuclear fuel
Uranium dioxide
Corrosion
H_2O_2 oxidation
Noble metal particles
Fission products

ABSTRACT

The anodic behaviour of simulated spent nuclear fuel (SIMFUEL) was studied in NaCl solutions containing H_2O_2 and various concentration of HCO_3^-/CO_3^{2-} using electrochemical, surface and solution analytical techniques. The two main anodic reactions are the oxidative dissolution of UO_2 and H_2O_2 oxidation. The relative importance of both reactions is controlled by the presence or absence of noble metal (ε) particles dispersed throughout the UO_2 matrix, the applied potential and the HCO_3^-/CO_3^{2-} concentration. Both reactions are suppressed by the formation of U^{VI} surface films. When the formation of these films is prevented at higher HCO_3^-/CO_3^{2-} concentrations, both reactions occur readily on the sublayer of $U^{IV}_{1-2x}U^{V}_{2x}O_{2+x}$. When present, noble metal (ε) particles support H_2O_2 oxidation over the full potential range. At low potentials the peroxycarbonate (HCO_4^-) species formed is rapidly oxidized on the particles. At high potentials H_2O_2 can be directly oxidized on the noble metal particles rendered catalytic by pre-oxidation (e.g., Pd to Pd^{II}).

1. Introduction

The universally accepted concept for the disposal of high-level nuclear waste, in particular spent nuclear fuel, is based on multiple barriers, including the fuel waste form, durable metal containers, a clay buffer and seals around the container, and a deep geologic repository (DGR) [1]. While such a DGR can provide acceptable assurance for long term containment, it is necessary to consider the consequences of container failure, which could lead to exposure of the fuel to groundwater. Since the spent fuel contains the radioactive fission and activation products, its behaviour in contact with groundwater provides the critical radioactivity source term in assessments of repository safety [2,3].

The chemistry/electrochemistry of UO_2 has been studied in a range of proposed repository conditions [4–11]. The redox condition of the groundwater contacting the fuel after container failure is the key factor likely to control the fuel corrosion rate, since the solubility of U is orders of magnitude higher for U^{VI} than for the reduced U^{IV} form [12]. If container failure occurs while significant radiation fields exist in the fuel, oxidizing conditions are expected to prevail near the fuel surface as a consequence of water radiolysis [9,13,14].

The radiation-induced dissolution of spent fuel has been investigated both experimentally and computationally [15–19], and the key oxidant has been shown to be H_2O_2 produced by the alpha radiolysis of the ground water [13,20,21]. The fate of H_2O_2 is either to be consumed where it is produced at the fuel surface, or to be transported away from the fuel surface and scavenged by available reducing species such as Fe^{2+} and H_2 produced by corrosion of the steel containment vessel. Fuel corrosion involves the coupling of UO_2 corrosion and H_2O_2 reduction [22,23],

$$H_2O_2 + 2e^- \rightarrow 2OH^- \quad (1)$$

$$UO_2 \rightarrow UO_2^{2+} + 2e^- \quad (2)$$

However, H_2O_2 can also undergo oxidation reaction 3, and the coupling of reaction 1 and 3 would lead to H_2O_2 decomposition to produce the alternative oxidant O_2.

$$H_2O_2 \rightarrow O_2 + 2H^+ + 2e^- \quad (3)$$

* Corresponding author. Department of Chemistry, The University of Western Ontario, London, Ontario, N6A 5B7, Canada.
E-mail address: jjnoel@uwo.ca (J.J. Noël).

https://doi.org/10.1016/j.electacta.2019.07.057

While an oxidant, O_2, would react over two orders of magnitude more slowly with UO_2 than the radiolytically produced H_2O_2 [4]. As indicated in Fig. 1, the relative importance of the two anodic reactions will determine the stability of UO_2 in H_2O_2 solutions.

Attempts have been made to determine the mechanistic balance between UO_2 dissolution and H_2O_2 decomposition under open circuit (corrosion) conditions. At low $[H_2O_2]$ ($<10^{-4}$ mol L^{-1}) the corrosion potential (E_{CORR}) increased from ~-0.4 V to ~ -0.1 V (vs. SCE) with increasing $[H_2O_2]$, and recent studies showed that the value of the steady-state E_{CORR} achieved was directly related to the extent of oxidation of the surface, as determined by X-ray photoelectron spectroscopy [24]. Over the intermediate $[H_2O_2]$ range, 10^{-4} to 5 $\times$ 10^{-3} mol L^{-1}, E_{CORR} rose rapidly to a final steady-state value (~0.1 V), indicating that the first stage of oxidation of the surface from $U^{IV}O_2$ to $U^{IV}_{1-2x}U^{V}_{2x}O_{2+x}$ was rapid. At potentials in this range, both oxidative dissolution as $U^{VI}O_2^{2+}$ and H_2O_2 decomposition are possible. Based on the independence of E_{CORR} from $[H_2O_2]$, it was claimed that the corrosion of the surface and the decomposition of H_2O_2 on the $U^{IV}_{1-2x}U^{V}_{2x}O_{2+x}$ layer were both limited by the slow dissolution of U^{VI} species from a U^{VI} surface layer. XPS measurements confirmed the presence of U^{VI} on the electrode in this potential range.

For $[H_2O_2] \geq 5 \times 10^{-3}$ mol L^{-1}, E_{CORR} increased approximately linearly with concentration, and coverage of the electrode by U^{VI} species increased. Experiments in which the amount of dissolved U^{VI} was measured showed that, at these higher $[H_2O_2]$, dissolution was accelerated [25,26], and the rate became first order with respect to $[H_2O_2]$. The increase in dissolution rate coupled to an apparently greater coverage by insulating and potentially blocking surface U^{VI} species was taken as an indication of enhanced dissolution at locally acidified sites on the electrode surface [27]. How these changes influenced the rate and mechanism of H_2O_2 decomposition was not investigated. A similar mechanism was proposed for the influence of α-radiolytically produced H_2O_2 on UO_2 corrosion and H_2O_2 decomposition [13]. It has also been claimed that, in the presence of both H_2O_2 and HCO_3^-/CO_3^{2-} at high concentrations, UO_2 corrosion is accelerated by the formation of a soluble peroxycarbonate complex, $U^{VI}O_2(O_2)_x(CO_3)_y^{2-2x-2y}$ [28,29].

While the cathodic reduction of H_2O_2 on UO_2 has been investigated [22,23,26,30,31], the kinetics of H_2O_2 oxidation and its relative importance when accompanied by the anodic dissolution of UO_2 has received minimal attention. Wu et al. [32] studied the anodic behaviour on a SIMFUEL electrode in HCO_3^-/CO_3^{2-} solutions containing various concentrations of H_2O_2. The rates of both anodic reactions were found to be at least partially controlled by the chemical release of U^{VI} surface species as $U^{VI}O_2(CO_3)_x^{(2-2x)+}$, and H_2O_2 oxidation appeared to be the dominant reaction, although a quantitative separation was not achieved. In addition, the role of the noble metal (ε) particles, known to exist in spent fuel and present in the SIMFUEL used [33,34], on these anodic reactions remains unknown.

In this study, the mechanisms of both the anodic reactions are investigated. The specific goals are the following: (i) to determine the mechanisms of both reactions; (ii) to determine their relative importance as a function of potential and carbonate concentration ($[CO_3]_{tot}$); and (iii) to elucidate the role played by noble metal (ε) particles in determining the relative importance of anodic dissolution and H_2O_2 decomposition.

2. ii) Experimental

2.1. a. Electrode materials and preparation and solutions

SIMFUELs are UO_2 pellets doped with non-radioactive elements to replicate the chemical effects of in-reactor irradiation [35]. Two different SIMFUEL samples were used in this study: one doped with 11 elements (Sr, Y, Ce, Nd, La, Zr, Ba, Pd, Ru, Mo, Rh) to simulate a fuel with both a rare earth-doped lattice and noble metal (ε) particles, designated (RE + ε), and a second one not containing the noble metal elements (Pd, Ru, Rh, Mo) and hence free of ε-particles, designated RE. The SIMFUELs were fabricated and supplied by Atomic Energy of Canada Ltd. (Chalk River, Canada).

All solutions were prepared with Type-1 water (resistivity, ρ = 18.2 MΩ cm) purified using a Millipore milli-Q-plus unit to remove organic and inorganic impurities. Experiments were conducted in a 0.1 mol L^{-1} NaCl solution containing 0.02 mol L^{-1} H_2O_2 with the pH adjusted to 9.7 with NaOH. $NaHCO_3$ was added to a concentration ($[CO_3]_{tot}$) in the range 0.01–0.1 mol L^{-1}. All chemicals were reagent grade and purchased from Fisher Scientific.

2.2. b. Electrochemical cell and equipment

Experiments were conducted using a three-compartment, three-electrode electrochemical cell. The reference electrode was a commercial saturated calomel electrode (SCE) (0.242 V vs. SHE) at 20 °C. The counter electrode was a Pt foil spot-welded to a Pt wire. The cell was placed in a Faraday cage to minimize interference from external noise. The rotation rate of the rotating disc electrode (RDE) was controlled using an analytical rotator from Pine Instruments (model ASR). All the electrochemical experiments were performed with a Solartron 1287 potentiostat controlled by CorrWare Version 2.7 software. The electrode resistivity (ρ (RE) = 174 Ω cm; ρ (RE + ε) = 81 Ω cm) was compensated using the current interrupt procedure [36].

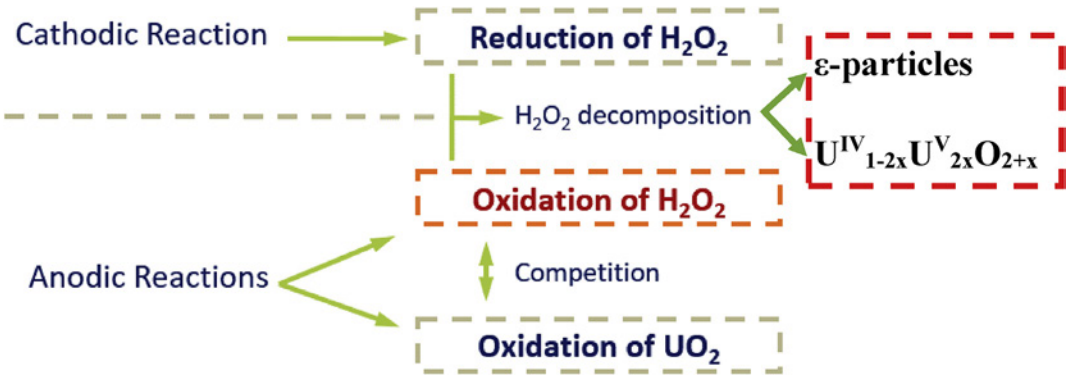

Fig. 1. Schematic illustration of the possible reactions of H_2O_2 on a UO_2 surface, showing that the H_2O_2 oxidation reaction can be catalyzed by a UO_{2+x} surface or by noble metal (ε) particles.

2.3. c. Electrochemical Experiments

Before each experiment, the SIMFUEL electrode was wet polished with 1200 grit SiC paper and rinsed with Millipore water. The working electrode was then cathodically cleaned at a potential of −1.2 V for 2 min prior to each experiment. For potentiostatic experiments, the working electrodes were oxidized for 10 min at a potential in the range of 0.1–0.4 V until a steady-state current was achieved. In dissolution experiments, the working electrode was held at each potential for 1 h.

In these experiments, the electrodes were oxidized for 1 h either at the corrosion potential (E_{CORR}) or at a positive applied potential (E) (0.2, 0.3 or 0.4 V). The amount of dissolved U in the solution was then measured and converted into an equivalent charge using Faraday's Law,

$$m = QM/Fn \quad (4)$$

where m is the mass reacted, Q is the electrochemical charge equivalent to the amount of U dissolved, F is Faraday's constant (96 485 C mol^{-1}), and n is the number of electrons involved in the dissolution reaction (2 for $U^{IV} \rightarrow U^{VI}$). After anodic oxidation for 1 h, the electrode was quickly transferred to a H_2O_2-free solution for cathodic stripping voltammetry (CSV) to estimate the amount of charge consumed in the production of surface oxidized layers.

2.4. d. Electrode surface and solution analyses

2.4.1. i. Inductively Coupled Plasma Atomic Emission Spectroscopy (ICP-AES)

The concentration of U in the solution was analyzed by inductively coupled plasma atomic emission spectroscopy (ICP-AES). These analyses were performed with a PerkinElmer Optima 3300 Dual 24 View ICP-AES located in the Biotron facility (Western University). The U emission was monitored at a wavelength of 419 nm, with a detection limit of 0.01 mg L^{-1}. Prior to injection into the spectrometer, samples were mixed with 2% HNO_3 to prevent U precipitation. The calibration standards used were 0.5, 1.0, and 5.0 mg L^{-1} U solutions, and a 2% HNO_3 solution was used as a blank sample.

2.4.2. ii. Scanning electron microscopy (SEM) and energy dispersive X-ray spectroscopy (EDX)

The surface morphology of the electrode was obtained using a Hitachi S-4500 field emission scanning electron microscope equipped with a Quartz XOne energy dispersive X-ray analyzer located at Surface Science Western (SSW). Immediately after an experiment, samples were rinsed with Millipore H_2O and dried in an Ar stream prior to being placed in the microscope. The electron beam potential was maintained at 5.0–15 keV and the working distance was 10 mm during image collection, resulting in a spatial resolution of <2 nm. Micrographs were recorded at various magnifications (100 − 5000X).

2.4.3. iii. Raman spectroscopy

Raman spectra were obtained using a Renishaw 2000 Laser Raman spectrometer (Renishaw PLC., UK) equipped with a Leica DMLM microscope. Spectra were excited using a He-Ne laser with a wavelength of 632.8 nm. The laser beam was focused to ~2 μm in diameter with a 50x uncoated objective lens on to the electrode mounted on carbon tape attached to a glass slide. The power of the laser beam was kept at 50% to avoid laser heating effects. The spectrometer was calibrated with a standard Si wafer, which has an intense Raman band at 520 cm^{-1}. Spectra were measured over the wavenumber range of 120–1400 cm^{-1}. After the measurements, the Gaussian-Lorentzian peak model and a Shirley baseline correction were used to fit the Raman peaks. The deconvolution of the broad band at 500-700 cm^{-1} has been described in detail elsewhere [37,38].

3. iii) Results and discussion

3.1. a. Cyclic voltammetry

Fig. 2 shows CVs recorded on the two electrodes in a 0.1.mol L^{-1} NaCl solution containing 0.02 mol L^{-1} of $NaHCO_3$ (pH = 9.7). In the absence of H_2O_2, Fig. 2 A, there was no significant difference between the two electrodes in the anodic region. However, the cathodic current increased significantly at −0.8 V on the RE + ε electrode due to the catalysis of H_2O reduction on the noble metal (ε) particles. When H_2O_2 was added to the solution, Fig. 2 B, the anodic current was significantly enhanced and reached a maximum at 0.27 V on the RE electrode with the decreases at positive potential indicating the formation of corrosion products on the UO_2 surface and the inhibition of one or both of the anodic oxidation

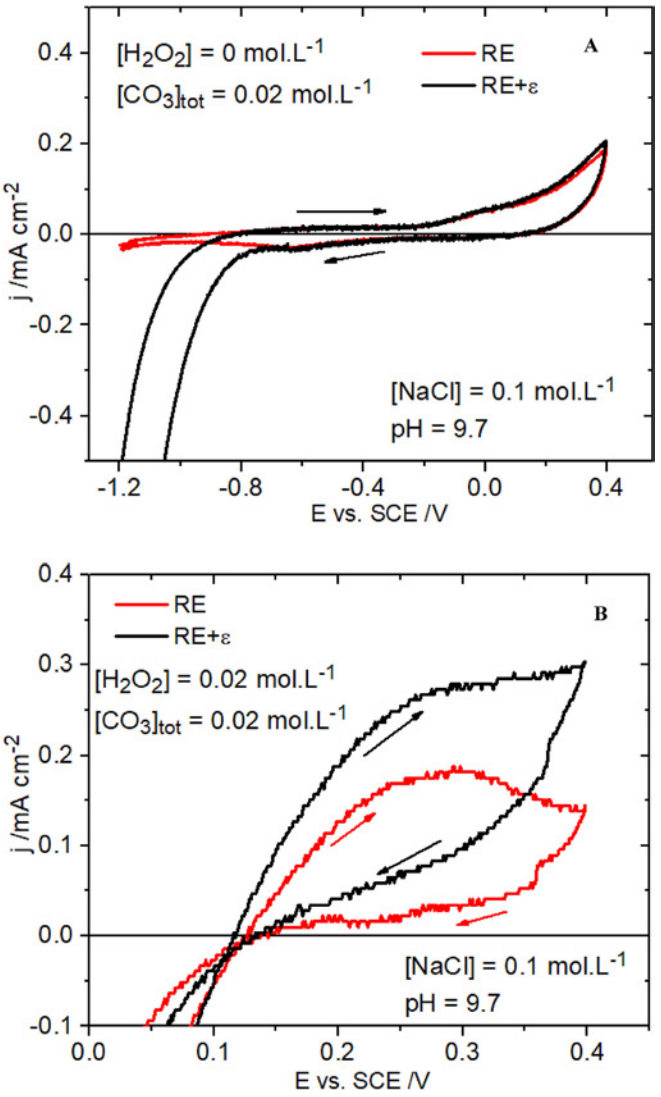

Fig. 2. CVs recorded on the RE and RE+ε electrodes in an Ar-sparged 0.1 mol L^{-1} NaCl solution containing 0.02 mol L^{-1} $NaHCO_3$ with a pH of 9.7, (A) without H_2O_2; (B) with 0.02 mol L^{-1} H_2O_2: the electrode rotation rate was 16.7 Hz.

processes. On the RE + ε electrode, the current was further enhanced and no peak was observed at the positive potential limit of the scan. This enhancement suggested a role for the ε-particles in determining the anodic current over the full potential range shown.

3.2. b. Characterization of noble metal (ε) particles

3.2.1. i. SEM and EDX

Fig. 3 shows the surface morphology of the RE + ε and RE electrodes. The RE + ε electrode (Fig. 3 A) featured distinct particles mainly residing on grain boundaries and possessed a smaller grain size than the RE electrode. The EDX analyses, Fig. 4, showed that the distinct particles contained Ru, Pd, Rh and Mo, consistent with previous analyses [35]. A more extensive analysis of the composition of a number of ε-particles in the RE + ε electrode showed their composition to be Pd (40 ± 6%), Ru (29 ± 5%), Rh (14 ± 3%) and Mo (15 ± 4%) [39].

3.2.2. ii. Raman analyses

Fig. 5 shows representative Raman spectra recorded on the RE and RE + ε electrode surfaces. These spectra exhibit a number of bands [37].

(i) The dominant peak at 445 cm^{-1} can be attributed to the fundamental U-O stretching mode of the fluorite lattice.
(ii) A band at 1150 cm^{-1} (not shown) has been assigned as an overtone (2L-O) of the first order L-O phonon observed at 570-575 cm^{-1} [40].
(iii) The broad band between 500 and 700 cm^{-1} can be attributed to UO_2 lattice damage, due to the formation of defects caused by lattice doping.

The band in this last region was deconvoluted into three peaks at 540 cm^{-1}, 570 cm^{-1} and 640 cm^{-1}. The peak at 570 cm^{-1} was attributed to a first order phonon (as noted above) while the peak at 540 cm^{-1} was attributed to the creation of oxygen vacancies (O_V) [41,42] in response to the need for charge compensation due to RE^{III} doping, a process which appears to involve the formation of RE^{III}-O_V clusters.

A peak at 640 cm^{-1} has been commonly assigned to distortion of the anion sublattice associated with a vibrational mode involving clusters of interstitial O atoms in a non-stoichiometric UO_{2+x} lattice. Since the SIMFUELs used in these experiments were sintered and reduced they were expected to be stoichiometric, making this assignment of the peak at 640 cm^{-1} unlikely. It has been suggested [38] this peak can be attributed to a Zr-O_8 complex since Zr^{IV} doping would cause a decrease in the UO_2 lattice parameter, a feature that would be expected to lead to lattice stabilization against anodic oxidation.

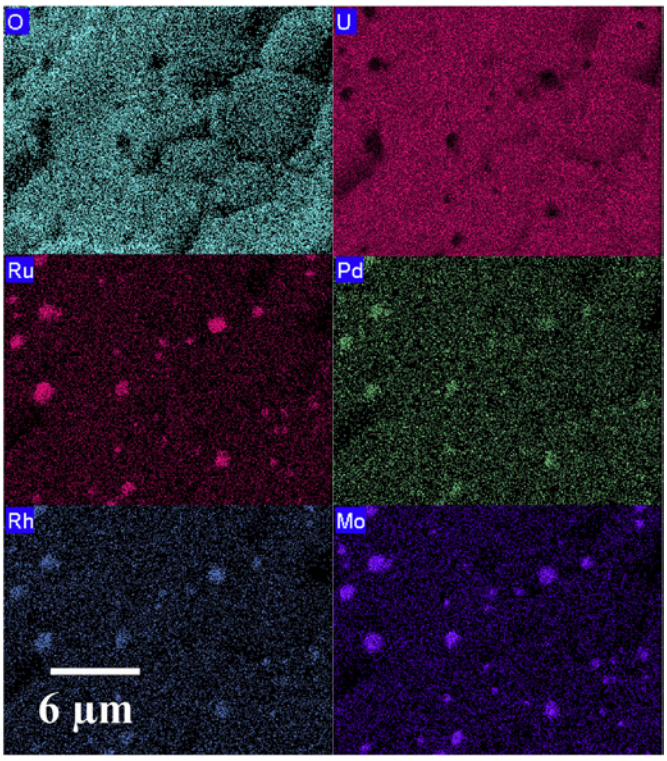

Fig. 4. EDX maps recorded on the RE+ε electrode showing the distribution of noble metal dopants (Ru, Pd, Ru, and Mo).

Since the peak at 445 cm^{-1} is characteristic of the undisturbed fluorite lattice and the 540 cm^{-1} peak can be attributed to the creation of O_V associated with RE^{III}-doping, the area ratio of these two peaks has commonly been used as a measure of the number of such vacancies [38]. Fig. 6 shows the peak areas normalized to the area of the peak at 445 cm^{-1}. If it is accepted that the ratio of the 540 cm^{-1} and 445 cm^{-1} peak areas is a measure of the number of O_V created by RE^{III} doping, then the RE electrode appeared to have a slightly higher density of O_V than the RE + ε electrode.

3.3. c. Steady-state currents at various $[CO_3]_{tot}$

Fig. 7 shows the current densities recorded on both electrodes over a range of E in a 0.1 mol L^{-1} NaCl solution containing 0.1 mol L^{-1} of $[CO_3]_{tot}$ and 0.02 mol L^{-1} of H_2O_2. The current reached a steady-state value rapidly on both electrodes, but slightly

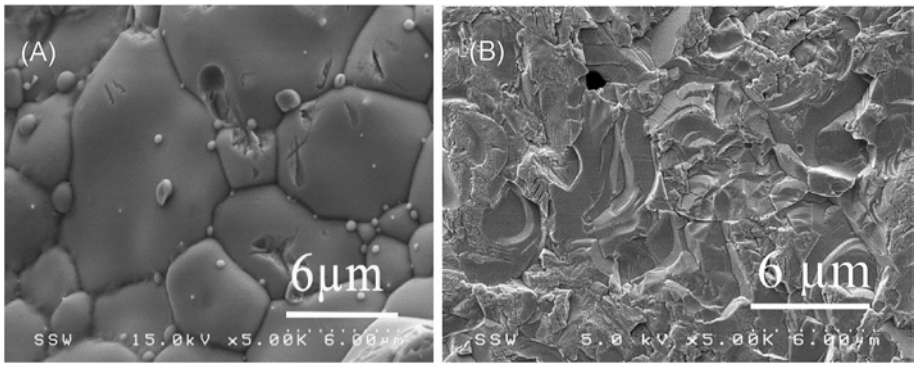

Fig. 3. SEM images of (A) the RE + ε electrode; (B) the RE electrode.

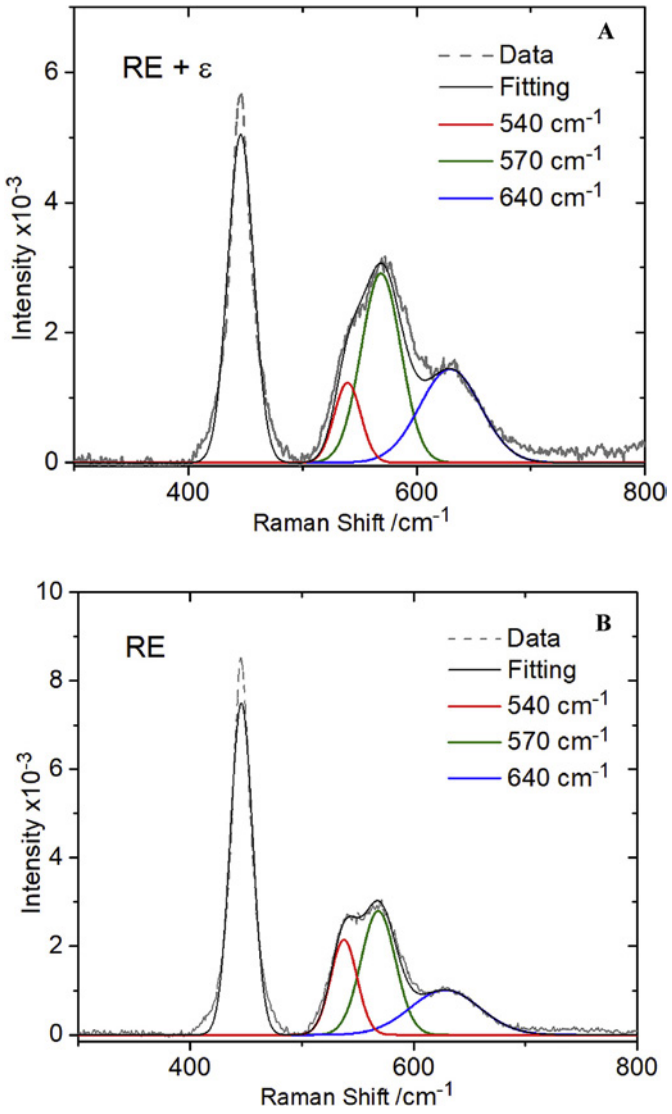

Fig. 5. Raman spectra recorded on the freshly polished (A) RE + ε and (B) RE SIMFUEL electrodes.

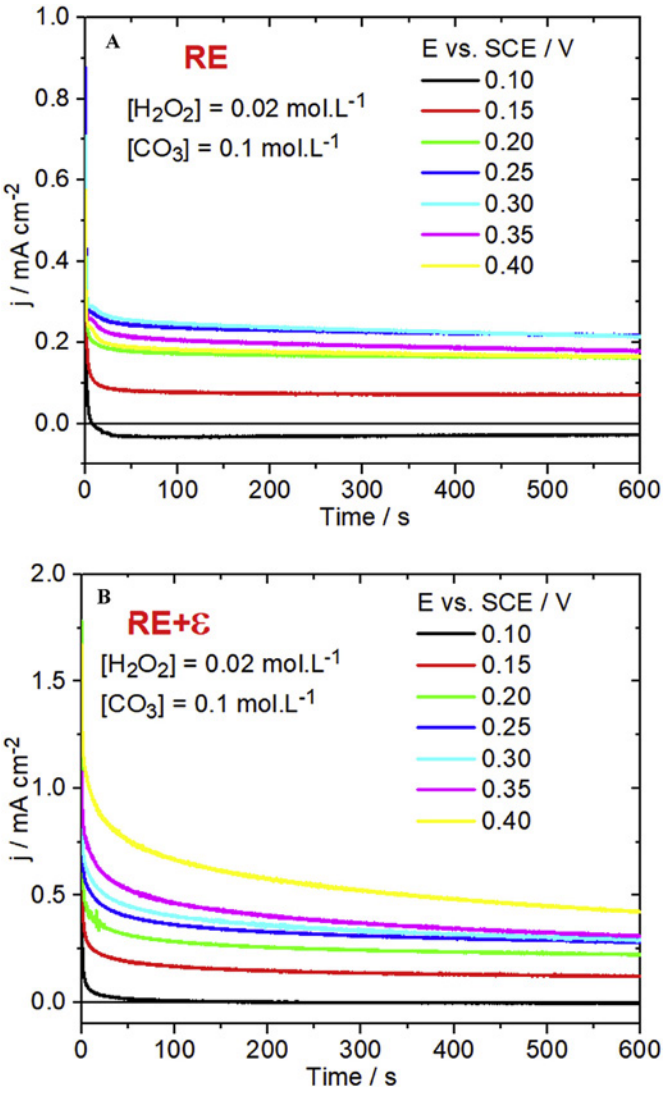

Fig. 7. Current densities measured at different E for 10 min on (A) the RE, and (B) the RE+ε electrodes in an Ar-purged 0.1 mol L^{-1} NaCl solution containing 0.1 mol L^{-1} $[CO_3]_{tot}$ and 0.02 mol L^{-1} H_2O_2, pH = 9.7, electrode rotation rate = 16.7 Hz.

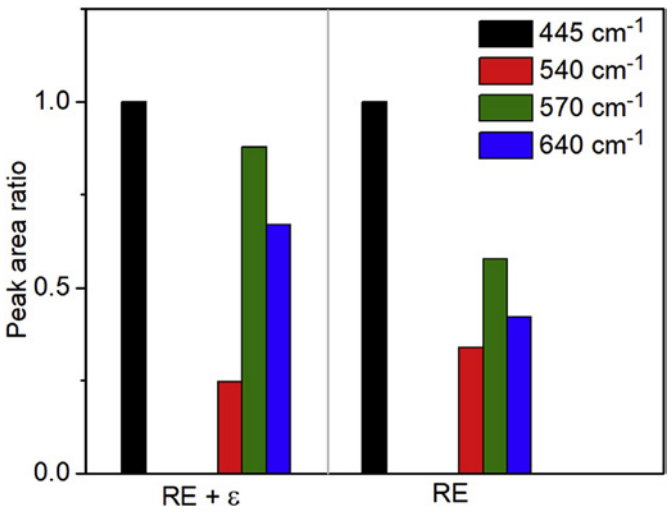

Fig. 6. Comparison of Raman peak areas normalized to the area of the 445 cm^{-1} peak recorded on the RE + ε and RE electrodes.

more rapidly on the RE electrode especially at the higher E.

Fig. 8 A and B show the steady-state currents plotted against E. On the RE electrode, the current exhibited the same dependence on E as observed voltammetrically, Fig. 7, increasing over the low potential range before decreasing again at higher E. The decrease in current beyond the peak became less marked as $[CO_3]_{tot}$ was increased. On the RE + ε electrode, the current showed a similar behaviour at low E, but any tendency to decrease at more positive E was overcome by a further current increase for E > 0.3 V.

Fig. 8C shows the difference between the currents (Δj) recorded on the two electrodes,

$$\Delta j = j_{RE+\varepsilon} - j_{RE} \quad (5)$$

Since the key difference between the two electrodes is the presence of noble metal (ε) particles in the RE + ε electrode, this suggested Δj could be attributed to reactions occurring on these particles, not on the UO_2 surface. As will be demonstrated below, the second possibility, that the anodic reactivities of the two doped UO_2 matrices are different, can be ruled out. The enhanced currents on the RE + ε, given by Δj, Fig. 8C, can be divided into two distinct

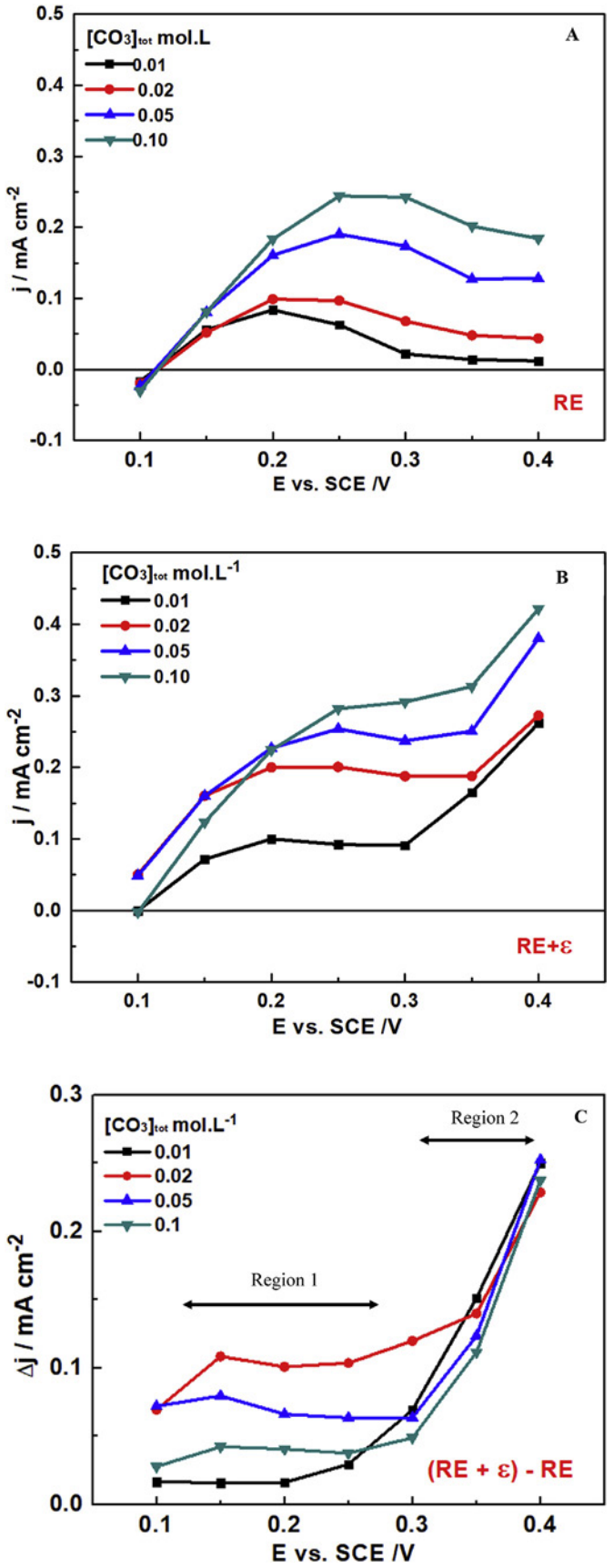

Fig. 8. Steady-state oxidation current densities as a function of E recorded on the (A) RE and (B) RE+ε electrodes in an Ar-purged 0.1 mol L^{-1} NaCl solution containing 0.02 mol L^{-1} H_2O_2, and various $[CO_3]_{tot}$ from 0.01 mol L^{-1} to 0.1 mol L^{-1}, (C) calculated current density difference, $j_{(RE+\varepsilon)} - j_{RE}$, determined from (A) and (B); pH = 9.7, electrode rotation rate = 16.7 Hz.

regions: (i) For sufficiently low E, Δj became independent of E, while clearly dependent on $[CO_3]_{tot}$; (ii) As E was increased, Δj increased steeply with E and became independent of $[CO_3]_{tot}$.

3.4. d. Anodic dissolution of UO_2

The currents recorded in the potentiostatic experiments, Figs. 7 and 8, contain contributions from both UO_2 and H_2O_2 oxidation. To separate these contributions, the electrodes were potentiostatically oxidized at different applied potentials for 1 h and the solutions then analyzed for dissolved U. In addition, the charge consumed by the formation of the oxidized surface layers, $U^{IV}_{1-2x}U^{V}_{2x}O_{2+x}$ and $U^{VI}O_3.yH_2O$ and possibly studtite ($U^{VI}O_4 \cdot 4H_2O$, which could form in the presence of H_2O_2 [19,42–44]) was determined by cathodic stripping voltammetry. This charge was found to be negligible compared to the total anodic charge consumed and was not, therefore, taken into consideration.

Fig. 9 shows that the amount of U dissolved was almost identical for both electrodes, irrespective of the $[CO_3]_{tot}$. Despite the differences in the total amount of charge consumed, obtained by integration of the current over the 1 h duration of the experiment, the data in Fig. 9 show that the extent of U dissolution was similar on the RE and RE + ε electrodes. This demonstrates that the extent of dissolution was uninfluenced by the presence of noble metal (ε) particles, and hence not responsible for the differences in anodic current, Δj (Fig. 8C). Also, this similarity in U^{VI} release rates confirmed that the slight differences in the number of RE^{III}-O_V clusters indicated by the Raman analyses had minimal influence on the anodic reactivity of the UO_2 matrix. This is consistent with previous observations on the influence of RE^{III} doping on the anodic reactivity [45].

SEM micrographs recorded on the RE + ε electrode, Fig. 10, showed some etching of the surface, possibly with some enhanced grain boundary dissolution. Although not shown, similar changes in surface morphology were observed on the RE electrode.

At E_{CORR}, the amount of U^{VI} dissolved was effectively independent of $[CO_3]_{tot}$, Fig. 9, indicating that the slow step in the overall dissolution process was the anodic formation of the U^{VI} species from the preformed U^{IV}/U^{V} surface layer

$$U^{IV}O_2 \rightarrow U^{IV}_{1-2x}U^{V}_{2x}O_{2+x} \rightarrow \left(U^{VI}\right)_{surf} \rightarrow U^{VI}O_2(CO_3)_y^{(2-2y)+} \quad 6$$

At higher E and low $[CO_3]_{tot}$, only a marginal increase in U^{VI} release was observed prior to the inhibition of release at high E (0.3 V, 0.4 V), when the surface became covered with a $U^{VI}O_3 \cdot yH_2O$ film, although the formation of studtite ($U^{VI}O_4 \cdot 4H_2O$) was also possible in the presence of H_2O_2. [19,42–44] This suppression of dissolution at high E on the RE electrode was consistent with the low currents observed at 0.3/0.4 V (Fig. 8 A), which demonstrates that the anodic oxidation of H_2O_2 was also suppressed at these potentials. By contrast, the suppression of U^{VI} dissolution on the RE + ε electrode under these conditions, Fig. 9, was not accompanied by a decrease in current, Fig. 8 B, confirming that the higher currents at 0.3/0.4 V were due to an increase in the anodic oxidation of H_2O_2 on the noble metal (ε) particles.

At higher $[CO_3]_{tot}$, the intermediate $U^{IV}_{1-2x}U^{V}_{2x}O_{2+x}$ layer was considerably thinner and anodic dissolution proceeded more rapidly through U^{V}/U^{VI} surface intermediates [46].

$$U^{IV}O_2 + HCO_3^- \rightarrow U^{V}O_2(HCO_3)_{ads} + e^- \quad 7$$

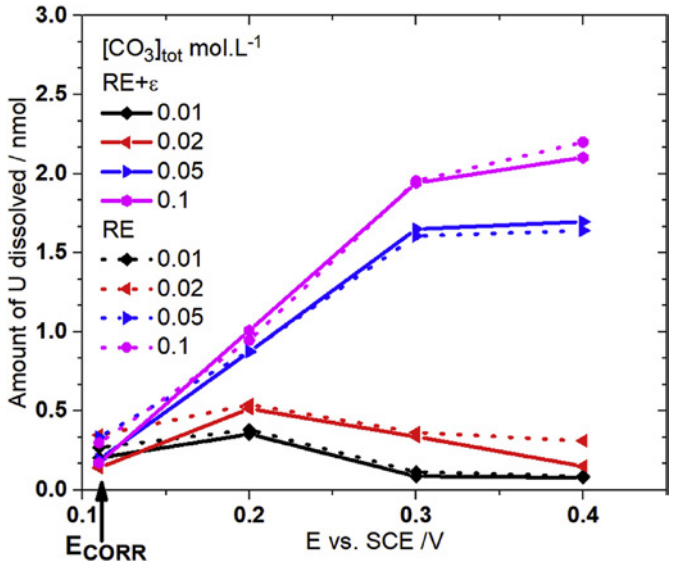

Fig. 9. The amount of U dissolved at E_{CORR} and various E values (1 h) for both RE and RE+ε electrodes.

$$U^{V}O_2(HCO_3)_{ads} + OH^- \rightarrow U^{VI}O_2(CO_3)_{ads} + H_2O + e^- \quad 8$$

$$U^{VI}O_2(CO_3)_{ads} + HCO_3^- \rightarrow U^{VI}O_2(CO_3)_2^{2-} + H^+ \quad 9$$

At low E, the amount of U^{VI} released increased with E indicating control of the dissolution reaction by reaction 8. For E > 0.3 V, the amount released became independent of E but exhibited a dependence on $[CO_3]_{tot}$ consistent with a switch in rate control to the final chemical dissolution (reaction 9). It is possible that this dissolution reaction was accelerated by the formation of a soluble peroxycarbonate complex, $U^{VI}O_2(O_2)_x(CO_3)_y^{2-2x-2y}$. The formation of such a species was shown to accelerate UO_2 dissolution when H_2O_2 and HCO_3^-/CO_3^{2-} concentrations were higher than those employed in this study [28,29].

Based on these analyses, the total charge consumed by anodic dissolution (Q_{UO2}) was calculated and compared to the total amount of anodic charge. The ratio of these charges is plotted in Fig. 11. which provides a measure of the relative importance of U^{VI} dissolution. On the RE electrode, the ratio (i.e., the importance of dissolution) increased with E for all $[CO_3]_{tot}$, as indicated by the green arrow, Fig. 11, with dissolution becoming the dominant reaction at 0.4 V despite the overall decrease in current, Fig. 8A, and the suppression of U^{VI} release, Fig. 9, particularly at low $[CO_3]_{tot}$.

These results confirmed that the formation of U^{VI} surface films strongly suppressed the anodic oxidation of H_2O_2. However, the dependence on $[CO_3]_{tot}$ at both 0.3 V and 0.4 V, in particular the latter, peaked at intermediate $[CO_3]_{tot}$ (0.02 mol L^{-1}) before decreasing again at higher concentrations, as indicated by the red arrows in Fig. 11 A. This suggested two influences of HCO_3^-/CO_3^{2-}: (i) at the two low $[CO_3]_{tot}$ an increase leads to a significant promotion of the importance of anodic dissolution, confirming that the increased anodic current can be attributed to an acceleration in the rate of the electrochemical reaction 8; (ii) at the higher $[CO_3]_{tot}$ (0.05 and 0.1 mol L^{-1}) the relative importance of the dissolution reaction was decreased; i.e., the relative importance the anodic oxidation of H_2O_2 increased, once the surface U^{VI} layer was rapidly dissolved and the conductive underlying $U^{IV}_{1-2x}U^{V}_{2x}O_{2+x}$ layer exposed.

Significantly different behaviour was observed on the RE + ε electrode. At low $[CO_3]_{tot}$ the ratio decreased to 3.5% as E was increased to 0.4 V, as indicated by the green arrow in Fig. 11. This decrease accompanied the overall decrease in U^{VI} release, Fig. 9, and the accompanying increase in anodic current, Fig. 8 B and Fig. 8C, confirming the dominance of H_2O_2 oxidation under these conditions. Since the surface of the UO_2 matrix remained protected by the U^{VI} surface film at low $[CO_3]_{tot}$, these observations clearly

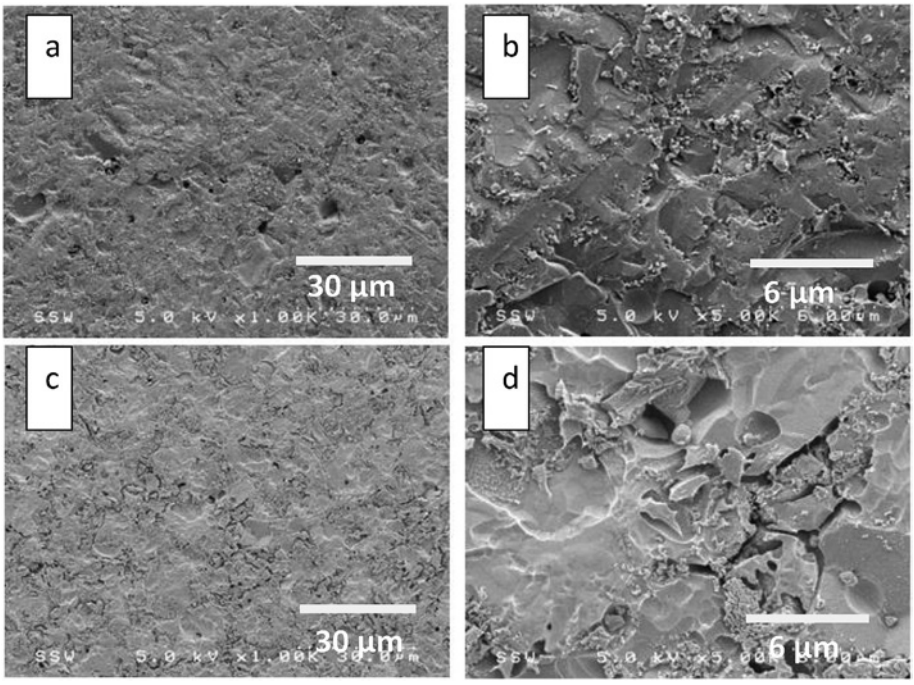

Fig. 10. SEM micrographs of the RE + ε electrode before and after anodic oxidation at E = 0.35 V for 1 h in a solution of 0.1 mol L^{-1} NaCl, 0.02 mol L^{-1} H_2O_2 and 0.1 mol L^{-1} $NaHCO_3$ with pH = 9.7: (a) and (b), the freshly polished electrode; (c) and (d) the surface of the electrode after anodic oxidation at 0.35 V for 1 h.

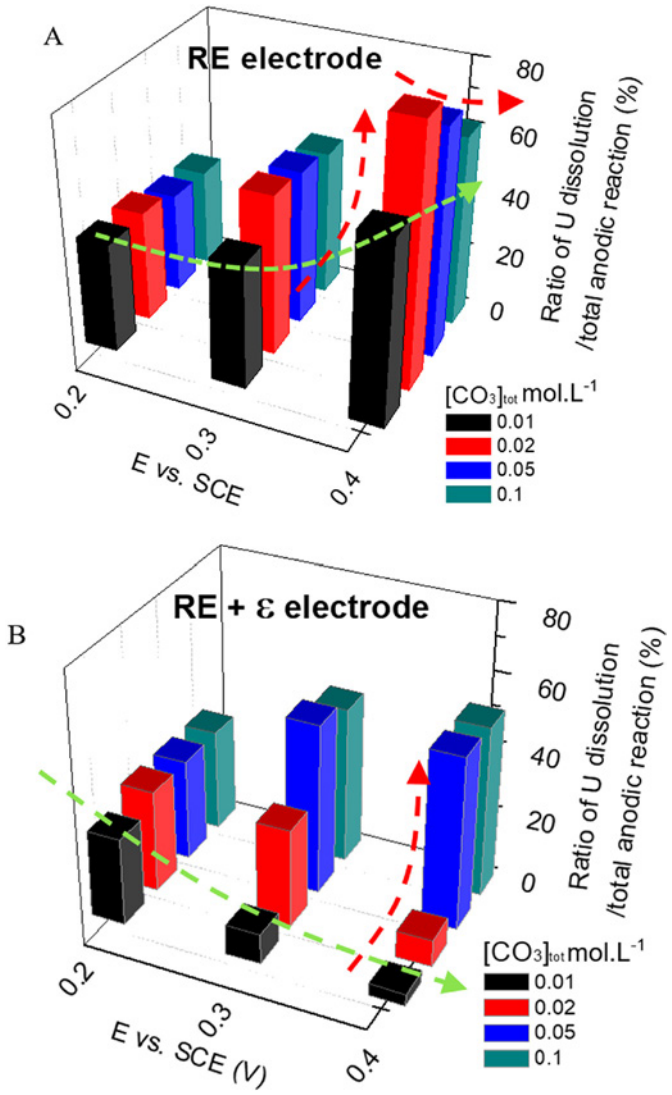

Fig. 11. The ratio of the charge consumed by UO_2 dissolution to the total electrochemical charge consumed calculated for (A) the RE electrode, and (B) the RE+ε electrode as a function of E and $[CO_3]_{tot}$.

demonstrated that the acceleration of H_2O_2 oxidation was supported on the noble metal (ε) particles. At higher $[CO_3]_{tot}$ the relative importance of U^{VI} dissolution was revived as the U^{VI} surface film dissolved, as indicated by the red arrow in Fig. 11 B.

3.5. e. The anodic oxidation of H_2O_2

The importance of H_2O_2 oxidation, and the influence of $[CO_3]_{tot}$ and E on it, are demonstrated in Fig. 12, which shows the anodic charge due to H_2O_2 oxidation (Q_{H2O2}) calculated by subtracting the charge due to UO_2 dissolution (Q_{UO2}) from the total electrochemical charge. At low E (0.2 V), Q_{H2O2} increased with $[CO_3]_{tot}$ on both electrodes. This, and the observation that the current for H_2O_2 oxidation on noble metal (ε) particles was enhanced in this potential region 1 (Fig. 8C), demonstrated that HCO_3^-/CO_3^{2-} influenced H_2O_2 oxidation in two ways: (i) as discussed above it accelerated U^{VI} dissolution leading to the exposure of the conductive $U^{IV}_{1-2x}U^{V}_{2x}O_{2+x}$ sublayer on which H_2O_2 oxidation could occur; (ii) it accelerated H_2O_2 oxidation on the noble metal (ε) particles in region 1 (Fig. 8C).

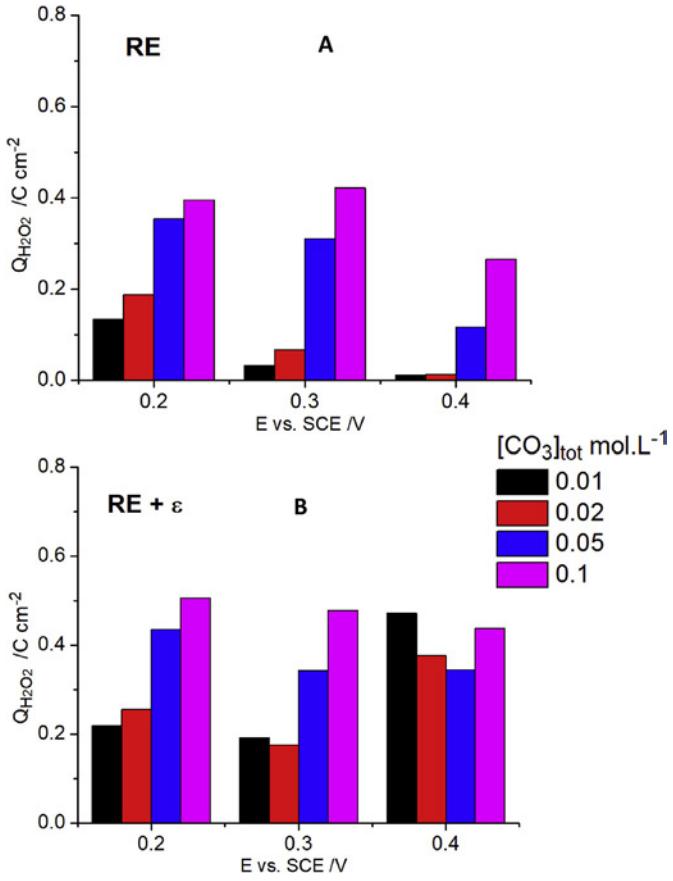

Fig. 12. The anodic charge due to H_2O_2 oxidation ($\mathbf{Q_{H_2O_2}}$) as a function of E on the RE (A) and RE+ε (B) electrodes in a $[NaCl] = 0.1\ mol\ L^{-1}$ solution containing $[H_2O_2] = 0.02\ mol\ L^{-1}$ and various $[CO_3]_{tot}$.

This dependence of the current and the charge for H_2O_2 oxidation on $[CO_3]_{tot}$ indicated that a carbonate-mediated oxidation of H_2O_2 was occurring on the noble metal (ε) particles in potential region 1 (Fig. 8C). The combination of H_2O_2 and HCO_3^-/CO_3^{2-} is known to form a reactive peroxycarbonate species,

$$HCO_3^- + H_2O_2 \rightarrow HCO_4^- + H_2O \quad 10$$

a reaction which can catalyze H_2O_2 decomposition and is known to enhance its reactivity [47]. Once formed, its anodic oxidation to O_2 and the regeneration of HCO_3^- was rapid on the noble metal (ε) particles,

$$2HCO_4^- \rightarrow 2HCO_3^- + O_2 + 2e^- \quad 11$$

On the RE electrode, the ability of HCO_3^-/CO_3^{2-} to revive H_2O_2 oxidation by dissolving the insulating U^{VI} surface layers to expose the underlying catalytic $U^{IV}_{1-2x}U^{V}O_{2+x}$ layer was clear, Q_{H2O2} increasing with $[CO_3]_{tot}$ at all three potentials.

While the value of Q_{H2O2} also increased with $[CO_3]_{tot}$ on the RE + ε electrode, the extent of H_2O_2 oxidation was much greater at 0.4 V than it was on the RE electrode, and the excess current, Δj, showed that the reaction was not dependent on $[CO_3]_{tot}$, although it was occurring on the noble metal (ε) particles. This can be attributed to the direct oxidation of H_2O_2 on the noble metal (ε) particles, this reaction having been shown to be catalyzed by oxidized states on the surface of noble metals [48–52], e.g., Pd^{II} on Pd,

$$Pd + 2H_2O \rightarrow Pd^{II}(OH)_2 + H^+ + 2e^- \quad 12$$

$$Pd^{II}(OH)_2 + H_2O_2 \rightarrow Pd^{II}(OH)_2(H_2O_2)_{ads} \quad 13$$

$$Pd^{II}(OH)_2(H_2O_2)_{ads} \rightarrow Pd + O_2 + 2H_2O \quad 14$$

4. iv) Summary

Fig. 13 shows a schematic summary of the reactions occurring on the various features and surface states on the UO_2/ε-particle surface.

- At all potentials, including E_{CORR}, the surface was covered by a thin conductive $U^{IV}_{1-2x}U^{V}_{2x}O_{2+x}$ layer able to support both anodic dissolution of the UO_2 matrix and anodic oxidation of H_2O_2.
- The balance between these anodic reactions varied with, (i) the presence or absence of noble metal (ε) particles dispersed throughout the fission product-doped UO_2 matrix, (ii) the potential applied, and (iii) the $[CO_3^{2-}]_{tot}$.
- At low $[CO_3]_{tot}$ both anodic reactions were retarded by the growth of insulating U^{VI} surface layers, and the rate of the anodic oxidation of H_2O_2 became controlled by the rate of the release of U^{VI} to solution to expose the underlying conductive $U^{IV}_{1-2x}U^{V}_{2x}O_{2+x}$ layer.
- The dissolution of this thin U^{VI} layer was accelerated in the presence of HCO_3^-/CO_3^{2-}, leading to increases in the rate of both anodic reactions.
- The presence of noble metal (ε) particles did not influence the anodic dissolution of the UO_2 matrix but offered an additional pathway for the anodic oxidation of H_2O_2.
- At low potentials, in the presence of HCO_3^-/CO_3^{2-}, a peroxycarbonate species, HCO_4^- was formed and rapidly oxidized to O_2 on the particles.
- At high potentials, H_2O_2 was directly oxidized on the noble metal (ε) particles, which were rendered catalytic by their electrochemical oxidation (e.g., Pd → Pd^{II}).

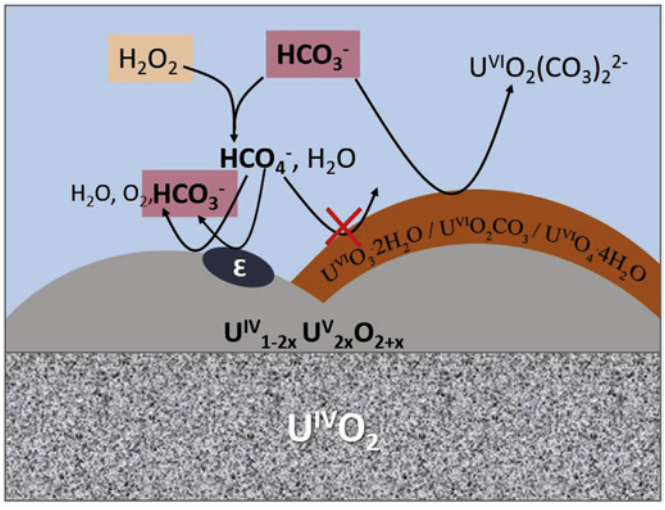

Fig. 13. Schematic illustration of the major reactions occurring on the RE and RE+ ε electrode surfaces in solutions containing H_2O_2 and CO_3^{2-}/HCO_3^-.

Acknowledgements

This research was funded under the Industrial Research Chair and Collaborative Research and Development (CRDPJ 507465–16) agreements between the Natural Sciences and Engineering Research Council (NSERC, Ottawa) and the Nuclear Waste Management Organization (NWMO, Toronto).

Appendix A. Supplementary data

Supplementary data to this article can be found online at https://doi.org/10.1016/j.electacta.2019.07.057.

References

[1] J. McMurry, D. Dixon, J. Garroni, B. Ikeda, S. Stroes-Gascoyne, P. Baumgartner, T. Melnyk, Evolution of a Canadian Deep Geologic Repository: Base Scenario, Ontario Power Generation Report, 2003, pp. 01200–10092.
[2] F. Garisto, Fourth Case Study: Features, Events and Processes, Nuclear Waste Management Organization, Canada, 2012.
[3] L. Werme, C. Lilja, Fuel and Canister Process Report for the Safety Assessment SR-Site, Swedish Nuclear Fuel and Waste Management Co. (SKB), Stockholm, Stockholm, 2010. Report TR-10-46.
[4] D.W. Shoesmith, Fuel corrosion processes under waste disposal conditions, J. Nucl. Mater. 282 (2000) 1–31.
[5] L.H. Johnson, D.W. Shoesmith, in: W. Lutze, R.C. Ewing (Eds.), Radioactive Waste Forms for the Future, Elsevier Science Publishers: North-Holland, Amsterdam, 1988.
[6] L.O. Werme, L. Johnson, V. Oversby, F. King, K. Spahiu, B. Grambow, D. Shoesmith, Spent Fuel Performance under Repository Conditions: A Model for Use in SR-Can, SKB2004.
[7] C. Poinssot, C. Ferry, M. Kelm, J. Cavedon, C. Corbel, C. Jegou, P. Lovera, F. Miserque, A. Poulesquen, B. Grambow, Spent Fuel Stability under Repository Conditions-Final Report of the European Project, CEA Saclay, 2005.
[8] J. Bruno, Spent Nuclear Fuel, Elements (Quebec) 2, 2006, pp. 343–349.
[9] D. Shoesmith, Used Fuel and Uranium Dioxide Dissolution Studies–A Review, Report NWMO TR-2007-03, Nuclear Waste Management Organization, Toronto, ON, 2007.
[10] H. He, M. Broczkowski, K. O'Neil, D. Ofori, O. Semenikhin, D. Shoesmith, Corrosion of Nuclear Fuel (UO_2) inside a Failed Nuclear Waste Container, Nuclear Waste Management Organization, Toronto, Ontario, 2012.
[11] N. Liu, Z. Zhu, J.J. Noël, D.W. Shoesmith, Corrosion of Nuclear Fuel inside a Failed Waste Container, Encyclopedia of Interfaical Chemistry: Surface Science and Electrochemistry, 2018.
[12] I. Grenthe, J. Fuger, R.J. Konings, R.J. Lemire, A.B. Muller, C. Nguyen-Trung, H. Wanner, Chemical Thermodynamics of Uranium, 1992. North-Holland Amsterdam.
[13] J. Wren, D. Shoesmith, S. Sunder, Corrosion behavior of uranium dioxide in alpha radiolytically decomposed water, J. Electrochem. Soc. 152 (2005) B470–B481.
[14] K. Spahiu, D. Cui, M. Lundström, The fate of radiolytic oxidants during spent fuel leaching in the presence of dissolved near field hydrogen, Radiochim 92 (2004) 625–629.
[15] K. Ollila, V.M. Oversby, Dissolution of Unirradiated UO_2 and UO_2 Doped with ^{233}U under Reducing Conditions, Swedish Nuclear Fuel and Waste Management Co., 2005.
[16] B. Muzeau, C. Jégou, F. Delaunay, V. Broudic, A. Brevet, H. Catalette, E. Simoni, C. Corbel, Radiolytic oxidation of UO_2 pellets doped with alpha-emitters (238/239Pu), J. Alloy. Comp. 467 (2009) 578–589.
[17] M. Jonsson, F. Nielsen, O. Roth, E. Ekeroth, S. Nilsson, M.M. Hossain, Radiation induced spent nuclear fuel dissolution under deep repository conditions, Environ. Sci. Technol. 41 (2007) 7087–7093.
[18] O. Roth, M. Trummer, M. Jonsson, Factors influencing the rate of radiation-induced dissolution of spent nuclear fuel, Res. Chem. Intermed. 35 (2009) 465–478.
[19] G. Sattonnay, C. Ardois, C. Corbel, J.F. Lucchini, M.F. Barthe, F. Garrido, D. Gosset, Alpha-radiolysis effects on UO_2 alteration in water, J. Nucl. Mater. 288 (2001) 11–19.
[20] C.M. Lousada, M. Trummer, M. Jonsson, Reactivity of H_2O_2 towards different UO_2-based materials: the relative impact of radiolysis products revisited, J. Nucl. Mater. 434 (2013) 434–439.
[21] T.E. Eriksen, D.W. Shoesmith, M. Jonsson, Radiation induced dissolution of UO_2 based nuclear fuel – a critical review of predictive modelling approaches, J. Nucl. Mater. 420 (2012) 409–423.
[22] J.S. Goldik, H.W. Nesbitt, J.J. Noël, D.W. Shoesmith, Surface electrochemistry of UO_2 in dilute alkaline hydrogen peroxide solutions, Electrochim. Acta 49 (2004) 1699–1709.
[23] J.S. Goldik, J.J. Noël, D.W. Shoesmith, The electrochemical reduction of hydrogen peroxide on uranium dioxide electrodes in alkaline solution, J. Electroanal. Chem. 582 (2005) 241–248.

[24] M. Razden, Electrochemical and Surface Compositional Studies on Uranium Dioxide, PhD Thesis, Chemistry Department, The University of Western Ontario, 2013.
[25] H. Christensen, E. Bjergbakke, Radiation induced dissolution of UO_2, MRS Proceedings 84 (1986) 115.
[26] J. Giménez, E. Baraj, M.E. Torrero, I. Casas, J. de Pablo, Effect of H_2O_2, NaClO and Fe on the dissolution of unirradiated UO_2 in NaCl 5 mol kg^{-1}. Comparison with spent fuel dissolution experiments, J. Nucl. Mater. 238 (1996) 64–69.
[27] S. Sunder, N.H. Miller, D.W. Shoesmith, Corrosion of uranium dioxide in hydrogen peroxide solutions, Corros. Sci. 46 (2004) 1095–1111.
[28] S.M. Peper, L.F. Brodnax, S.E. Field, R.A. Zehnder, S.N. Valdez, W.H. Runde, Kinetic study of the oxidative dissolution of UO_2 in aqueous carbonate media, Ind. Eng. Chem. Res. 43 (2004) 8188–8193.
[29] G.S. Goff, L.F. Brodnax, M.R. Cisneros, S.M. Peper, S.E. Field, B.L. Scott, W.H. Runde, First identification and thermodynamic characterization of the ternary U (VI) species, $UO_2(O_2)(CO_3)_2^{4-}$, in UO_2–H_2O_2–K_2CO_3 solutions, Inorg. Chem. 47 (2008) 1984–1990.
[30] M. Trummer, S. Nilsson, M. Jonsson, On the effects of fission product noble metal inclusions on the kinetics of radiation induced dissolution of spent nuclear fuel, J. Nucl. Mater. 378 (2008) 55–59.
[31] B.G. Santos, J.J. Noël, D.W. Shoesmith, The effect of pH on the anodic dissolution of SIMFUEL (UO_2), J. Electroanal. Chem. 586 (2006) 1–11.
[32] G.J.S. Wu L, D.W. Shoesmith, The anodic reactions on simulated spent fuel (SIMFUEL) in H_2O_2 solutions: effect of carbonate/bicarbonate, J. Electrochem. Soc. 161 (2014) C363–C371.
[33] H. Kleykamp, R. Pejsa, X-ray diffraction studies on irradiated nuclear fuels, J. Nucl. Mater. 124 (1984) 56–63.
[34] H. Kleykamp, The solubility of selected fission products in UO_2 and (U, Pu) O_2, J. Nucl. Mater. 206 (1993) 82–86.
[35] P.G. Lucuta, R.A. Verrall, H. Matzke, B.J. Palmer, Microstructural features of SIMFUEL — simulated high-burnup UO_2-based nuclear fuel, J. Nucl. Mater. 178 (1991) 48–60.
[36] M.E. Broczkowski, J.J. Noël, D.W. Shoesmith, The influence of dissolved hydrogen on the surface composition of doped uranium dioxide under aqueous corrosion conditions, J. Electroanal. Chem. 602 (2007) 8–16.
[37] H. He, D. Shoesmith, Raman spectroscopic studies of defect structures and phase transition in hyper-stoichiometric $UO_{(2+x)}$, Phys. Chem. Chem. Phys. 12 (2010) 8108–8117.
[38] M. Razdan, D.W. Shoesmith, Influence of trivalent-dopants on the structural and electrochemical properties of uranium dioxide (UO_2), J. Electrochem. Soc. 161 (2014) H105–H113.
[39] M. Broczkowski, The Effects of Hydrogen and Temperature on the Electrochemistry and Corrosion of Uranium Dioxide, PhD Thesis, Chemistry Department, The University of Western Ontario, 2008 (Chapter 7).
[40] T. Livneh, E. Sterer, Effect of pressure on the resonant multiphonon Raman scattering in UO_2, Phys. Rev. B 73 (2006), 085118.
[41] L. Li, F. Chen, J.-Q. Lu, M.-F. Luo, Study of defect sites in Ce1−xMxO2−δ (x = 0.2) solid solutions using Raman spectroscopy, J. Phys. Chem. A 115 (2011) 7972–7977.
[42] L. Desgranges, Y. Pontillon, P. Matheron, M. Marcet, P. Simon, G. Guimbretière, F. Porcher, Miscibility gap in the U–Nd–O phase diagram: a new approach of nuclear oxides in the environment? Inorg. Chem. 51 (2012) 9147–9149.
[43] M. Amme, Contrary effects of the water radiolysis product H_2O_2 upon th dissolution of nuclear fuel in natural ground water and deionized water, Radiochim. Acta 90 (2002) 399–406.
[44] M. Amme, B. Renker, B. Schmid, M.P. Feth, H. Bertagnolli, W. Döbelin, Raman microspectrometric identification of corrosion products formed on UO_2 nuclear fuel during leaching experiments, J. Nucl. Mater. 306 (2002) 202–212.
[45] N. Liu, H. He, J.J. Noël, D.W. Shoesmith, The electrochemical study of Dy_2O_3 doped UO_2 in slightly alkaline sodium carbonate/bicarbonate and phosphate solutions, Electrochim. Acta 235 (2017) 654–663.
[46] P.G. Keech, J.S. Goldik, Z. Qin, D.W. Shoesmith, The anodic dissolution of SIMFUEL (UO_2) in slightly alkaline sodium carbonate/bicarbonate solutions, Electrochim. Acta 56 (2011) 7923–7930.
[47] T. Wu, J.D. Englehardt, A new method for removal of hydrogen peroxide interference in the analysis of chemical oxygen demand, Environ. Sci. Technol. 46 (2012) 2291–2298.
[48] S.B. Hall, E.A. Khudaish, A.L. Hart, Electrochemical oxidation of hydrogen peroxide at platinum electrodes. Part II: effect of potential, Electrochim. Acta 43 (1998) 2015–2024.
[49] J. Zhang, C. Lin, Z. Feng, Z. Tian, Mechanistic studies of electrodeposition for bioceramic coatings of calcium phosphates by an in situ pH-microsensor technique, J. Electroanal. Chem. 452 (1998) 235–240.
[50] L. Gorton, A carbon electrode sputtered with palladium and gold for the amperometric detection of hydrogen peroxide, Anal. Chim. Acta 178 (1985) 247–253.
[51] J.A. Cox, R.K. Jaworski, Voltammetric reduction and determination of hydrogen peroxide at an electrode modified with a film containing palladium and iridium, Anal. Chem. 61 (1989) 2176–2178.
[52] D.A. Johnston, M.F. Cardosi, D.H. Vaughan, The electrochemistry of hydrogen peroxide on evaporated gold/palladium composite electrodes, Manuf. Electrochem. Charact., Electroanal. 7 (1995) 520–526.